PHYSICAL REVIEW E **93**, 062217 (2016)

Breather transition dynamics, Peregrine combs and walls, and modulation instability in a variable-coefficient nonlinear Schrödinger equation with higher-order effects

Lei Wang,[1,*] Jian-Hui Zhang,[2] Chong Liu,[3] Min Li,[1] and Feng-Hua Qi[4]
[1]*Department of Mathematics and Physics, North China Electric Power University, Beijing 102206, People's Republic of China*
[2]*School of Energy Power and Mechanical Engineering, North China Electric Power University, Beijing 102206, People's Republic of China*
[3]*School of Physics, Northwest University, Xi'an 710069, People's Republic of China*
[4]*School of Information, Beijing Wuzi University, Beijing 101149, People's Republic of China*
(Received 11 March 2016; published 16 June 2016)

We study a variable-coefficient nonlinear Schrödinger (vc-NLS) equation with higher-order effects. We show that the breather solution can be converted into four types of nonlinear waves on constant backgrounds including the multipeak solitons, antidark soliton, periodic wave, and W-shaped soliton. In particular, the transition condition requiring the group velocity dispersion (GVD) and third-order dispersion (TOD) to scale linearly is obtained analytically. We display several kinds of elastic interactions between the transformed nonlinear waves. We discuss the dispersion management of the multipeak soliton, which indicates that the GVD coefficient controls the number of peaks of the wave while the TOD coefficient has compression effect. The gain or loss has influence on the amplitudes of the multipeak soliton. We further derive the breather multiple births and Peregrine combs by using multiple compression points of Akhmediev breathers and Peregrine rogue waves in optical fiber systems with periodic GVD modulation. In particular, we demonstrate that the Peregrine comb can be converted into a Peregrine wall by the proper choice of the amplitude of the periodic GVD modulation. The Peregrine wall can be seen as an intermediate state between rogue waves and W-shaped solitons. We finally find that the modulational stability regions with zero growth rate coincide with the transition condition using rogue wave eigenvalues. Our results could be useful for the experimental control and manipulation of the formation of generalized Peregrine rogue waves in diverse physical systems modeled by vc-NLS equation with higher-order effects.

DOI: 10.1103/PhysRevE.93.062217

I. INTRODUCTION

Breathers have gotten a lot of attention due to their interactions and energy exchange with a constant background [1,2]. Different from the usual soliton dynamics, their interactions can generate unique behaviors. Breathers can be classified into two kinds: Kuznetsov-Ma breathers (KMBs) [3] and Akhmediev breathers (ABs) [4]. KMBs are periodic in space and localized in time while ABs are periodic in time and localized in space. Taking the period of both breather solutions to infinity produces a Peregrine soliton (PS) solution [5], which is localized both in space and time and serves as a prototype of a rogue wave [6]. Rogue wave, which has a peak amplitude generally more than twice the significant wave height, appears from nowhere and disappears without a trace [2]. It appears as a result of the modulation instability (MI) [7,8] of a weakly modulated plane wave. And more specifically, rogue-wave formation is related to a special kind of MI, namely, the baseband MI whose bandwidth includes arbitrarily small frequencies [9]. Experimentally, rogue waves have been observed in optical fibers [10], water-wave tanks [11], and plasmas [12]. Despite that many integrable equations have been shown to admit the rogue-wave solutions, in theory, the standard nonlinear Schrödinger (NLS) equation is seen as a basic model for the dynamics of rogue waves, both in water and optics.

In optical communications, there always exist some nonuniformities due to various factors, which include the imperfection of manufacture, variation in the lattice parameters of the fiber media and fluctuation of the fiber diameters [13]. Those nonuniformities often lead to such effects as the fiber gain or loss, phase modulation, and variable dispersion [14]. The inclusion of the variable coefficients into the NLS equations is currently an effective way to reflect the inhomogeneous effects of the nonlinear optical pulses [15]. On the other hand, if the dispersion and nonlinear effect in a mode-locked fiber laser is very strong, the pulse parameters, such as the width, chirp, phase, and position, will change significantly from their initial values [16]. Thus, the concept of soliton dispersion management and soliton control in a fiber, which is used to address this problem, has been recently proposed. The dispersion management of the soliton is often modeled by the NLS equations with varying dispersion and nonlinear coefficients along with a gain or loss coefficient [17]. Serkin *et al.* reported for the first time the existence of a dispersion-managed soliton for such a system [17], and then showed some new results and predicted various applications of dispersion-management solitons [18]. Compared with a conventional soliton, this type of soliton can not only be accelerated but also be amplified, preserving its shape and elastic character, which makes it more suitable for diverse physical applications [16]. Different from the nonlinear evolution equations with constant coefficients, the rogue waves and breathers in variable-coefficient ones can show some novel features such as the nonlinear tunneling effect, recurrence, annihilation, and sustainment [19–21], to name a few. Recent studies have also reported the breather evolution, amplification, and compression, Talbot-like effects, and composite rogue-wave structures in some variable-coefficient nonlinear evolution equations [22]. Moreover, Tiofack *et al.* have demonstrated a novel multiple compression points structure in periodically modulated NLS equations, which is termed as a Peregrine

---

[*] 50901924@ncepu.edu.cn

comb [23]. Additionally, the studies of the control and manipulation of the rogue waves in variable-coefficient models may help to manage them experimentally in inhomogeneous optical fibers [21,24] and Bose-Einstein condensates [19,25], and also provide a good fit between the theoretical analysis and real applications in future spatial observations and laboratory plasma experiments [26].

The propagation of a picosecond optical pulse is usually described by the standard NLS equation. However, for the propagation of a subpicosecond or femtosecond pulse, the higher-order effects such as the third-order dispersion, self-steepening, and delayed nonlinear response should be taken into account [27–31], which makes the modification of the NLS equation as a more accurate prototype of the wave evolution in the real world. These effects may add qualitatively certain new properties to the wave propagation phenomena, e.g., to breathers, rogue waves, and MI. Akhmediev *et al.* have shown that a breather solution of the third- and fifth-order NLS equations can be converted into a nonpulsating soliton solution on a background, which does not exist in the standard NLS equation [32,33]. Wang *et al.* have discovered that the breather solutions in the NLS equation with fourth-order dispersion and nonlinear terms can be transformed into different types of nonlinear waves and the interactions between these waves are elastic [34]. Such transitions have also been reported in the higher-order coupled systems including the Hirota-Maxwell-Bloch (HMB) system [35] and NLS-MB system with fourth-order effects [36]. He *et al.* have found that the higher-order terms control compression effects of the breather and rogue waves [37]. With such higher-order perturbation terms as the third-order dispersion (TOD) and delayed nonlinear response term, Liu *et al.* have found that the MI growth rate shows a nonuniform distribution characteristic in the low perturbation frequency region, which opens up a stability region as the background frequency changes [38]. They have further exhibited an intriguing transition between bright-dark rogue waves and W-shaped–anti-W-shaped solitons, which occurs as a result of the attenuation of MI growth rate to vanishing in the zero-frequency perturbation region [39].

In this paper, we consider a variable-coefficient NLS (vc-NLS) equation with higher-order effects as follows [40–42]

$$i\,q_z + \frac{d_2(z)}{2}q_{tt} + R(z)|q|^2q - i\,d_3(z)q_{ttt} - i\,6\,\gamma(z)|q|^2q_t - \frac{i}{2}\Gamma(z)q = 0, \tag{1}$$

with

$$\frac{\gamma(z)}{d_3(z)} = \frac{R(z)}{d_2(z)}, \quad \Gamma = \frac{W[R(z),d_2(z)]}{d_2(z)R(z)}, \quad W[R(z),d_2(z)] = R\,d_{2z} - d_2\,R_z, \tag{2}$$

where z is the propagation variable, t is the retarded time in a moving frame with the group velocity, and $q(z,t)$ is the slowly varying envelope of the wave field. The coefficients $d_2(z)$, $R(z)$, $d_3(z)$, $\gamma(z)$, and $\Gamma(z)$ represent the group velocity dispersion (GVD) effect, Kerr nonlinear effect, TOD effect, the time-delay correlation to the cubic term, and the gain or loss effect, respectively. Liu *et al.* have studied the two-soliton interactions of Eq. (1) analytically and numerically, and discussed the higher-order-effects management of soliton interactions [41]. He *et al.* have investigated the control and manipulation of the rogue waves of Eq. (1) [42]. Note that the vector form of Eq. (1), i.e., the coupled Hirota equations, also admits the rogue wave [29,30], W-shaped soliton [39], and Peregrine comb solutions [43].

Our goals here are twofold: (i) the breather transition dynamics and nonlinear wave management; (ii) the breather multiple births and the Peregrine combs and walls. We first present intriguing different kinds of nonlinear localized and periodic waves, including the multipeak soliton, W-shaped soliton, and periodic wave. With the multipeak soliton, for example, we discuss the effects of GVD coefficient, TOD coefficient, and gain or loss coefficient. We further reveal the relation between such transition and MI characteristics. On the other hand, considering periodic modulation, we display three types of multiple compression points structures, the breather multiple births, Peregrine combs, and Peregrine walls, whose spatiotemporal characteristics are also analyzed analytically.

The arrangement of the paper is as follows. In Sec. II, we will present different types of transformed nonlinear waves of Eq. (1), show their interactions, and analyze the effects of variable coefficients. In addition, the transition condition will be given analytically. The relation between the MI growth rate and transition condition will be revealed in Sec. III. The Peregrine comb and wall structures as well as their spatiotemporal characteristics will be studied in Sec. IV. Finally, Sec. V will present the conclusions of this paper.

II. BREATHER TRANSITION DYNAMICS

A. Breather-to-soliton transitions

In this section, we mainly study the breather transition dynamics for Eq. (1). By virtue of the Darboux transformation (see Appendix), the first-order breather solution of Eq. (1) can be derived as

$$q_B^{[1]} = c(z)\left(1 + 2\,\beta\,\frac{G_B^{[1]} + i\,H_B^{[1]}}{D_B^{[1]}}\right)e^{i\,\rho}, \tag{3}$$

with

$$\rho = m(z) + n\,t, \quad m(z) = \int\left(-\frac{1}{2}(n^2-2)d_2(z) - n(n^2-6)d_3(z)\right)dz,$$

$$G_B^{[1]} = k_1k_2\cos(z\,V_H + t\,h_R)\,\cosh(2\,\chi_I) - \cosh(z\,V_T + t\,h_I)\,\sin(2\,\chi_R),$$

$$H_B^{[1]} = \cos(2\,\chi_R)\,\sinh(z\,V_T + t\,h_I) + k_1k_2\sin(z\,V_H + t\,h_R)\,\sinh(2\,\chi_I),$$

$$
\begin{aligned}
D_B^{[1]} &= \cosh(z\,V_T + t\,h_I)\cosh(2\,\chi_I) - k_1 k_2 \cos(z\,V_H + t\,h_R)\sin(2\,\chi_R),\\
h &= 2\sqrt{1+\left(\lambda+\frac{n}{2}\right)^2} = h_R + i\,h_I, \quad k_1 = 1, \quad k_2 = \pm 1,\\
\varpi &= \left(t - \frac{1}{2}\int((n-2\,\lambda)d_2(z) + 2(-2+n^2-2\,n\,\lambda+4\,\lambda^2)d_3(z))dz\right)\frac{h}{2}\\
&= [t + \varpi_R(z) + i\,\varpi_I(z)]\frac{h}{2},\\
\chi &= \frac{1}{2}\arccos\frac{h}{2}, \quad c(z) = \sqrt{\frac{d_2(z)}{R(z)}} = \sqrt{\frac{d_3(z)}{\gamma(z)}} = \exp\left[\frac{1}{2}\Gamma(z)\right], \quad \lambda = \alpha + \beta\,i,\\
V_T &= 2[\varpi_R(z)\,h_I + \varpi_I(z)\,h_R], \quad V_H = 2[\varpi_R(z)\,h_R - \varpi_I(z)\,h_I].
\end{aligned}
$$

From the above expression, one can find that the breather solution (3) is composed of the hyperbolic functions $\sinh(z\,V_T + t\,h_I)$, $\cosh(z\,V_T + t\,h_I)$, and trigonometric functions $\sin(z\,V_H + t\,h_R)$, $\cos(z\,V_H + t\,h_R)$, where $\varpi_R(z) + \frac{\varpi_I(z)h_R}{h_I}$ and $\varpi_R(z) - \frac{\varpi_I(z)h_I}{h_R}$ are the corresponding velocities. The hyperbolic functions and trigonometric functions describe the localization and periodicity of the transverse distribution t of those waves, respectively. The nonlinear wave described by the solution (3) could be seen as a nonlinear superposition of a soliton and a periodic wave. The period of the breather along t-coordinate axis is determined by $\frac{\pi}{h_R}$, which is related to the eigenvalue $\lambda = \alpha + \beta\,i$. Compared with the Hirota equation with constant coefficients, the breather solution (3) of the inhomogeneous Hirota equation (1) includes the variable dispersion $[d_2(z)]$, nonlinearity $[R(z)]$, higher-order effects $[d_3(z)$ and $\gamma(z)]$, and gain or loss $[\Gamma(z)]$. More specifically, the intensity of the breather is controlled by $c(z) = \sqrt{\frac{d_2(z)}{R(z)}} = \sqrt{\frac{d_3(z)}{\gamma(z)}} = \exp[\frac{1}{2}\Gamma(z)]$, which means that we can manipulate the intensity by adjusting the gain or loss coefficient or the ratio of dispersion and nonlinearity. In addition, it is observed that V_T and V_H are associated with the GVD effect $d_2(z)$ and TOD effect $d_3(z)$ that affect the velocity of the breather. Thus, we will study the dynamics of the breather described by the solution (3) depending on the above parameters.

First, we show that the breather solution (3) can be converted into four types of nonlinear waves depending on the values of the velocity difference $\frac{\varpi_I(z)(h_R^2+h_I^2)}{h_R h_I}$. When $\varpi_I(z)(\frac{h_R^2+h_I^2}{h_R h_I}) \neq 0$ [or $\varpi_I(z) \neq 0$], the solution (3) characterizes the localized waves with breathing behavior on constant backgrounds (i.e., the breathers and rogue waves). Further, if $\alpha = -\frac{n}{2}$, we have the ABs with $|\beta| < 1$, the KMBs with $|\beta| > 1$, and the PS with $|\beta| = 1$. Those solutions have been obtained via the similarity transformation [42].

Conversely, if $\varpi_I(z) = 0$, the soliton and periodic wave in the solution (3) have the same velocity $\varpi_R(z)$. Further, we find that the case $\varpi_I(z) = 0$ is equivalent to the following condition

$$\frac{V_T}{h_I} = \frac{V_H}{h_R}, \tag{4}$$

i.e.,

$$n = 4\,\alpha - \frac{d_2(z)}{2\,d_3(z)}. \tag{5}$$

The condition (4) indicates that the extrema of trigonometric and hyperbolic functions in the solution (3) is located along the same straight lines in the (z,t) plane, which leads to the transformation of the breather into different types of nonlinear waves on constant backgrounds. The equivalent form of the condition (4), namely Eq. (5), involves four parameters: the frequency of plane wave n, the real part of the eigenvalue α, and the GVD effect $d_2(z)$ and TOD effect $d_3(z)$. When $d_2(z)$ is proportional to $d_3(z)$ $[d_2(z) = k\,d_3(z),\ k \neq 0]$, Eq. (5) has solutions. However, if $d_2(z) = k(z)\,d_3(z)$ [$k(z)$ is a function of z], Eq. (5) has no solution. This means that the constraint $d_2(z) = k\,d_3(z)$ is the necessary condition for the existence of transformed nonlinear waves. For a fixed n, increasing the value of $\frac{d_2(z)}{d_3(z)}$ results in an decrease of α. This is plotted in Fig. 1.

Under the transition condition (5), we exhibit four kinds of transformed nonlinear waves on constant backgrounds including the multipeak solitons [Figs. 2(a) and 2(b)], antidark soliton [Fig. 2(c)], periodic wave [Fig. 2(d)], and W-shaped soliton [Fig. 2(e)]. These types of nonlinear waves have been found not only in the scalar equations including Hirota equation [32], fourth-order NLS equation [34], fifth-order NLS equation [33], but also in the coupled systems such as the NLS-MB system [44], HMB system [35], and AB system [45]. The difference between Fig. 2(a) and Fig. 2(b) is that the former shows the single main peak while the latter displays double main peaks. In order to more clearly reveal the regularity of transformation between these two waves, we consider $|q(0,0)|^2_{zz}$ as a control variable. The maximum amplitude of $|q(z,t)|^2$ at (0,0) can be presented analytically

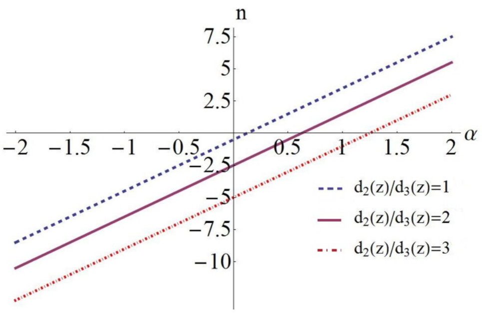

FIG. 1. Solutions of Eq. (5) on a plane of (n,α).

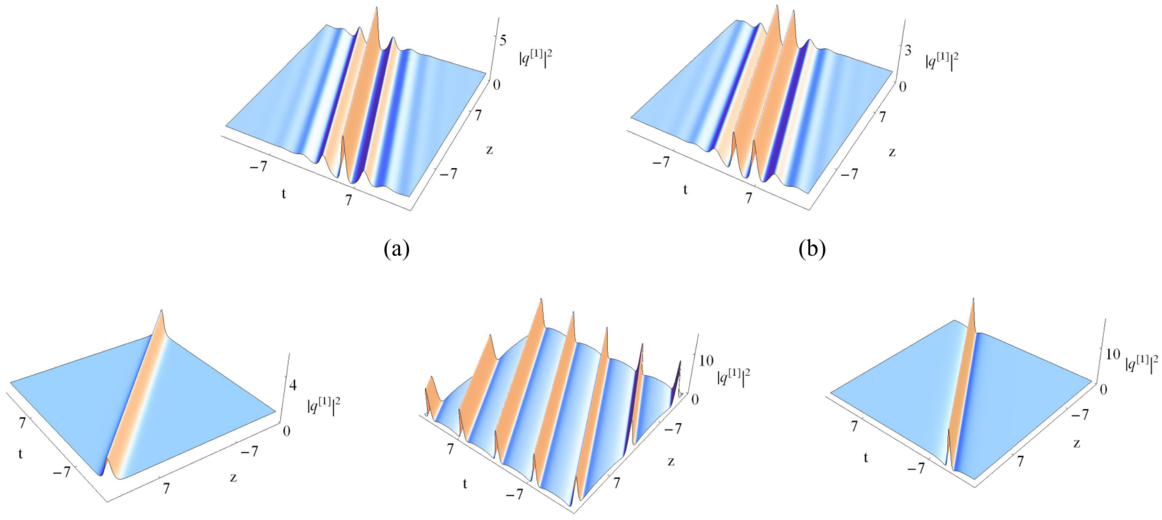

FIG. 2. Four types of transformed nonlinear waves with $R(z) = d_2(z) = d_3(z) = 0.1$. (a) Multipeak soliton (single main peak) with $k_1 = 1, k_2 = -1, \lambda_1 = \lambda_2^* = 0.2 + 0.6\,i$. (b) M-shaped soliton (double main peak) with $k_1 = 1, k_2 = -1, \lambda_1 = \lambda_2^* = 0.2 - 0.6\,i$. (c) Antidark soliton with $k_1 = k_2 = 1, \lambda_1 = \lambda_2^* = \frac{1}{12} + 1.4\,i$. (d) Periodic wave with $k_1 = 1, k_2 = -1, \lambda_1 = \lambda_2^* = \frac{1}{12} + 0.9\,i$. (e) W-shaped soliton with $k_1 = 1, k_2 = -1, \lambda_1 = \lambda_2^* = \frac{1}{12} + i$.

[in Fig. 2(a)],

$$|q(0,0)|^2 = \exp[\Gamma(z)](2\,\beta + 1)^2, \qquad (6)$$

which is related to the imaginary part of eigenvalue β and gain or loss $\Gamma(z)$. Unfortunately, due to the complexity of $|q(0,0)|^2_{zz}$, it is difficult to give its expression analytically. Thus, we only demonstrate the effect of β on $|q(0,0)|^2_{zz}$ numerically. As shown in Fig. 3, the green line ($-1.28 < \beta < 0$) corresponds to the case $|q(0,0)|^2_{zz} > 0$ that means the ordinate origin (0,0) is a minimum and the soliton has two main peaks with identical amplitude. Nevertheless, if the value of β exceeds a certain range, i.e., $\beta > 0$ or $\beta < -1.28$, the value of $|q(0,0)|^2_{zz}$ is less than zero, which results in the formation of one main peak. Consequently, the transition between these two kinds of waves can be governed by the imaginary part of eigenvalue β.

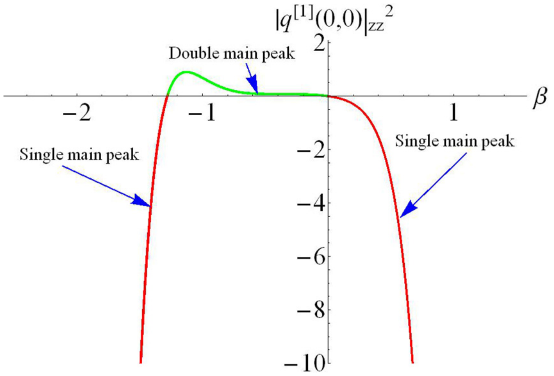

FIG. 3. Effects of the imaginary part of eigenvalue β on $|q(0,0)|^2_{zz}$ with $\delta_1 = \delta_2 = \delta_3 = 0.1, k_1 = 1, k_2 = -1$, and $\alpha = 0.2$. Two zeros of the $|q(0,0)|^2_{zz}$ are in (0,0) and $(-1.28,0)$ respectively. The green line corresponds to the double main peaks while the red line corresponds to the single peaks.

Next, we display two special nonlinear wave structures from the solution (3), i.e., the antidark soliton and periodic wave. The former exists in isolation when h_R vanishes, while the latter independently exists when h_I vanishes. Therefore, the antidark soliton and periodic wave are shown in forms of exponential and trigonometric functions respectively. Specifically, the analytical expressions read as, for the soliton,

$$q_S^{[1]} = c(z)\left(1 + 2\,\beta\,\frac{G_S^{[1]} + i\,H_S^{[1]}}{D_S^{[1]}}\right)e^{i\,\rho}, \qquad (7)$$

with

$$G_S^{[1]} = k_1 k_2\,\cosh(2\,\chi_I) - \cosh(z\,V_T + t\,h_I)\,\sin(2\,\chi_R),$$
$$H_S^{[1]} = \cos(2\,\chi_R)\,\sinh(z\,V_T + t\,h_I),$$
$$D_S^{[1]} = \cosh(z\,V_T + t\,h_I)\,\cosh(2\,\chi_I) - k_1 k_2\,\sin(2\,\chi_R),$$

and for the periodic wave,

$$q_P^{[1]} = c(z)\left(1 + 2\,\beta\,\frac{G_P^{[1]} + i\,H_P^{[1]}}{D_P^{[1]}}\right)e^{i\,\rho}, \qquad (8)$$

with

$$G_P^{[1]} = k_1 k_2 \cos(z\,V_H + t\,h_R)\,\cosh(2\,\chi_I) - \sin(2\,\chi_R),$$
$$H_P^{[1]} = k_1 k_2 \sin(z\,V_H + t\,h_R)\,\sinh(2\,\chi_I),$$
$$D_P^{[1]} = \cosh(2\,\chi_I) - k_1 k_2 \cos(z\,V_H + t\,h_R)\,\sin(2\,\chi_R).$$

The antidark soliton was first reported in the scalar NLS system with the third-order dispersion [46]. Recently, the similar structures have also been found in such coupled models as NLS-MB system [44], HMB system [35], and AB system [45]. The soliton depicted in Fig. 2(c) lies on a plane-wave background with a peak $c(z)^2(1 + 2\,\beta)^2$ and will become a standard bright soliton as $c(z) \to 0$. Figure 2(d)

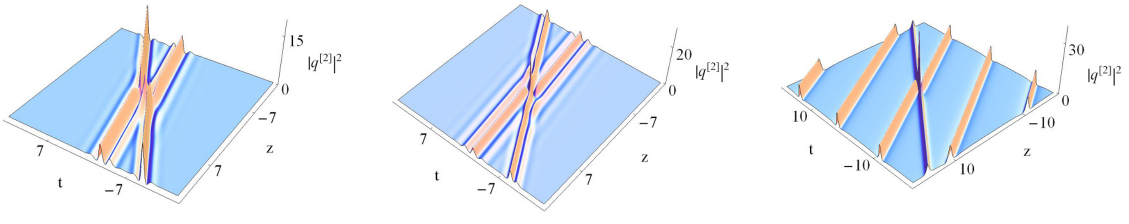

(a) (b) (c)

FIG. 4. The interactions between two nonlinear waves with $\delta_1 = \delta_2 = \delta_3 = 0.1$. (a) The collision between two multipeak solitons with $k_1 = k_2 = 1, \lambda_1 = \lambda_2^* = 0.5 + 1.2\,i, \lambda_3 = \lambda_4^* = 0.5 + 0.8\,i$. (b) The collision between two M-shaped solitons with $k_1 = 1, k_2 = -1, \lambda_1 = \lambda_2^* = 0.5 + 1.2\,i, \lambda_3 = \lambda_4^* = 0.5 + 0.6\,i$. (c) The collision between the antidark soliton and periodic wave with $k_1 = 1, k_2 = -1, \lambda_1 = \lambda_2^* = \frac{1}{12} + 1.6\,i, \lambda_3 = \lambda_4^* = \frac{1}{12} + 0.97\,i$.

shows the periodic wave with the period $P = \frac{\pi}{h_R}$. Interestingly, in spite of the same expression, the wave in Fig. 2(d) looks like a higher-order wave. When the period h_R is close to zero, namely, $\beta \to 1$, the periodic wave will reduce to a W-shaped soliton, as shown in Fig. 2(e). In this case, the solution (8) is transformed into

$$q_{RW}^{[1]} = \frac{144\, d_3(z)^2}{36\, d_3(z)^2 + [12\, d_3(z)\, t + z\, d_2(z)^2 + 72\, z\, d_3(z)^2]^2} + \exp\left[\frac{1}{2}\Gamma(z)\right] - 2, \tag{9}$$

which is referred to as the W-shaped soliton or a long-lived rogue wave.

We further derive the second-order transformed nonlinear waves. By means of the formulas (A7) with $N = 2$, the two-breather solution of Eq. (1) is given by

$$q_B^{[2]} = q^{[0]} - 2\,i\,\sqrt{\frac{d_2(z)}{R(z)}}\,\frac{\Delta_1^{[2]}}{\Delta^{[2]}}, \tag{10}$$

with

$$\begin{aligned}
&q^{[0]} = c(z)\, e^{i\,\rho},\\
&\lambda_1 = \lambda_2^* = \alpha_1 + \beta_1\, i, \quad \lambda_3 = \lambda_4^* = \alpha_2 + \beta_2\, i,\\
&\psi_2 = -\varphi_1^*, \quad \varphi_2 = \psi_1^*; \quad \psi_4 = -\varphi_3^*, \quad \varphi_4 = \psi_3^*;\\
&\varphi_j = k_1 \frac{-i\,h_j + 2\,i\,\lambda_j + i\,n}{2}\, e^{i\,(\varpi_j + \frac{\rho}{2})} + k_2\, e^{-i(\varpi_j - \frac{\rho}{2})},\\
&\psi_j = k_1\, e^{i\,(\varpi_j - \frac{\rho}{2})} + k_2 \frac{-i\,h_j + 2\,i\,\lambda_j + i\,n}{2}\, e^{-i(\varpi_j + \frac{\rho}{2})},\\
&\quad j = 1{,}3, \quad k_1 = 1, k_2 = \pm 1,\\
&\Delta_1^{[2]} = \begin{vmatrix} \lambda_1\varphi_1 & \varphi_1 & \lambda_1^2\varphi_1 & \psi_1\\ -\lambda_2\varphi_2 & -\varphi_2 & -\lambda_2^2\varphi_2 & \psi_2\\ \lambda_3\varphi_3 & \varphi_3 & \lambda_3^2\varphi_3 & \psi_3\\ -\lambda_4\varphi_4 & -\varphi_4 & -\lambda_4^2\varphi_4 & \psi_4 \end{vmatrix},\\
&\Delta^{[2]} = \begin{vmatrix} \lambda_1\varphi_1 & \varphi_1 & \lambda_1\psi_1 & \psi_1\\ -\lambda_2\varphi_2 & -\varphi_2 & \lambda_2\psi_2 & \psi_2\\ \lambda_3\varphi_3 & \varphi_3 & \lambda_3\psi_3 & \psi_3\\ -\lambda_4\varphi_4 & -\varphi_4 & \lambda_4\psi_4 & \psi_4 \end{vmatrix}.
\end{aligned}$$

By using the solution (10) and transition condition (5), we can obtain various nonlinear interactions among different types of transformed nonlinear waves. For more detailed analysis of these nonlinear interactions, one can refer to Refs. [34,35,39]. Here, we only exhibit a few typical examples. Figures 4(a)–4(c) describe the interactions between two multipeak solitons, and between the periodic wave and antidark soliton. We note that the collisions are elastic, i.e., the waves restore the original shapes, amplitudes, and velocities after each collision with a small phase shift. On the other hand, employing the semirational forms of the solution (10) and transition condition (5), we have the interactions between the W-shaped soliton and the antidark soliton, and between two W-shaped solitons, which are depicted in Fig. 5.

B. Dispersion management and nonlinear management

We discuss the effects of the variable coefficients on the nonlinear waves, i.e., the dispersion management and nonlinear management. Here we will pay attention to the multipeak soliton with single main peak. We omit the results on other types of nonlinear waves, since the effects of the variable coefficients on them are similar to the multipeak soliton with the same initial physical parameters. From the constraints (2), we note that five variable coefficients $d_2(z)$, $d_3(z)$, $R(z)$, $\gamma(z)$, and $\Gamma(z)$ are not independent of each other. The ratio of $d_2(z)$ and $R(z)$ must be equal to that of $d_3(z)$ and $\gamma(z)$. Additionally, $\Gamma(z)$ should be expressed by $d_2(z)$ and $R(z)$ [or $d_3(z)$ and $\gamma(z)$]. Therefore, we will consider dispersion management and nonlinear management of the multipeak soliton under the integrability condition (2).

We first study the effect of TOD coefficient $d_3(z)$ and time-delay correlation to the cubic term $\gamma(z)$ on the multipeak soliton. We fix the values of $d_2(z)$ and $R(z)$ while changing

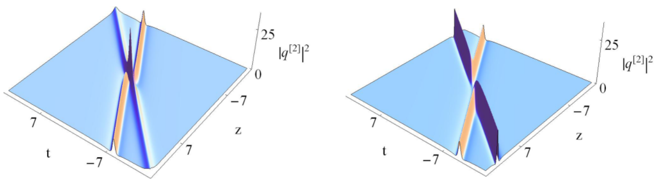

(a) (b)

FIG. 5. The interactions between two nonlinear waves with $\delta_1 = \delta_2 = \delta_3 = 0.1$. (a) The collision between W-shaped soliton and antidark soliton with $k_1 = k_2 = 1, \lambda_1 = \lambda_2^* = \frac{1}{12} + i, \lambda_3 = \lambda_4^* = \frac{1}{12} - 1.6\,i$. (b) The collision between two W-shaped solitons with $k_1 = k_2 = 1, \lambda_1 = \lambda_2^* = \frac{1}{12} + 1.2\,i, \lambda_3 = \lambda_4^* = \frac{1}{12} + 1.4\,i$.

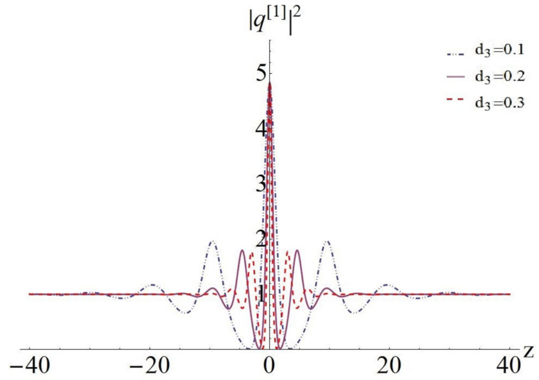

FIG. 6. The compression effect of TOD coefficient on the multipeak solitons with $\delta_1 = \delta_2 = 0.1, k_1 = 1, k_2 = -1, \lambda_1 = \lambda_2^* = 0.2 + 0.6\,i$.

the values of $d_3(z)$ and $\gamma(z)$. For simplicity, we set $\Gamma(z) = 0$. As shown in Fig. 6, we observe a compressed effect of the multipeak soliton by increasing the values of $d_3(z)$ and $\gamma(z)$. In other words, a further increase of the values of $d_3(z)$ and $\gamma(z)$ leads to stronger localization and a smaller oscillation period. However, the amplitudes of the multipeak soliton including the maximum and minimum ones do not change markedly, especially for the main peak. It is worth pointing out that we have to increase or decrease the values of $d_3(z)$ and $\gamma(z)$ simultaneously to ensure the integrability condition (2) to be true.

Second, we investigate how the GVD coefficient $d_2(z)$ and Kerr nonlinear coefficient $R(z)$ influence on the multipeak soliton. In this case, the values of $d_3(z)$ and $\gamma(z)$ cannot be changed and $d_2(z)$ and $R(z)$ are various. From Fig. 7, we discover that increasing the values of $d_2(z)$ and $R(z)$ also results in stronger localization and a smaller oscillation period for the multipeak soliton. More interestingly, different from the TOD effects, the GVD coefficient can affect the peak number of the multipeak soliton. When $d_2(z) = R(z) = 1$, the soliton has seven humps (see the dotted line in Fig. 7). By raising the values of $d_2(z)$ and $R(z)$, we can observe that the humps of the soliton increase from seven to thirteen (see the solid line in Fig. 7). Further, by comparing with the main peak, the amplitudes of secondary ones increase obviously.

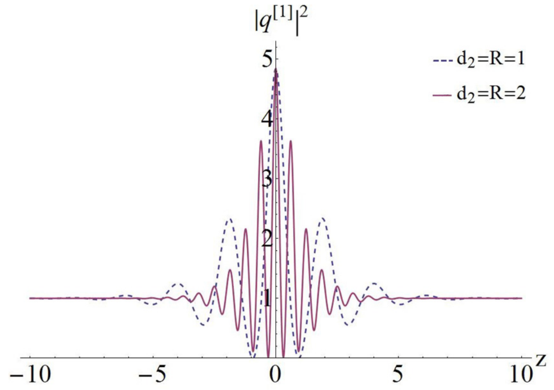

FIG. 7. The effects of GVD coefficient on the peak number of multipeak solitons with $\delta_3 = 0.1, k_1 = 1, k_2 = -1, \lambda_1 = \lambda_2^* = 0.2 + 0.6\,i$.

Third, we discuss the effects of the gain or loss coefficient $\Gamma(z)$. It should be pointed out that the GVD coefficient $d_2(z)$ and Kerr nonlinear coefficient $R(z)$ need to meet in a nonlinear relation [$d_2(z) = k(z)\,R(z)$, $k(z)$ is a function of z] because the case $d_2(z) = k\,R(z)$ will lead to the vanishing gain or loss effect. Based on the fact that decreasing GVD in a fiber has been realized, as an example, we consider an exponential dispersion decreasing fiber system with

$$d_2(z) = \delta_1 \exp(\xi\, z), \quad d_3(z) = \delta_3 \exp(\xi\, z), \tag{11}$$

$$R(z) = \delta_1, \quad \gamma(z) = \delta_3, \tag{12}$$

$$\Gamma(z) = \xi, \tag{13}$$

where δ_1 (δ_3) is the parameter related to the Kerr nonlinear (TOD) and ξ denotes the constant net gain or loss. Figure 8 describes the propagation of a multipeak soliton whose amplitudes, background, and velocity vary due to the nonvanishing gain or loss. From the expression (3), we see that the amplitudes of the multipeak soliton are determined by $c(z) = \exp(\frac{\xi}{2}\,z)$, and the velocity is influenced by $d_2(z) = \delta_1 \exp(\xi\, z), d_3(z) = \delta_3 \exp(\xi\, z)$. If $\xi > 0$, the amplitude of this wave will increase exponentially whereas it will decrease exponentially. In addition, we observe that the multipeak soliton is compressed during the propagation owing to the exponential dispersion decreasing coefficients. The cases $\xi < 0$ and $\xi > 0$, respectively, correspond to the compression and amplification.

Finally, we consider a soliton management system similar to that of Refs. [40,47], i.e., the periodic distributed system

$$R(z) = \delta_1 \sin(\xi\, z), \quad d_2(z) = \delta_2 \sin(\xi\, z),$$
$$d_3(z) = \delta_3 \sin(\xi\, z), \quad \gamma(z) = \frac{\delta_1 \delta_3}{\delta_2} \sin(\xi\, z). \tag{14}$$

Trigonometric functions are physically relevant because they provide for alternating regions of positive and negative dispersion and nonlinearity, indicated in the improved stability of the solitons [10]. The periodically accelerating or decelerating multipeak soliton are shown in Fig. 9(a). The two solitons in Fig. 9(b) propagate with periodic oscillation along the time z, and the separated solitons collide periodically.

Let us then discuss briefly the possible observation and applicability of the analytic results of breather transition dynamics above. As is well known, the integrable Hirota model can be regarded as a special case for the femtosecond optical pulse propagation in a fiber [48]. Therefore, our results could be of importance to study different types of optical excitations arising from the higher-order effects exactly. Recently, optical rogue waves and breathers have been realized in a fiber by the initial intensity and phase modulations extracting from the exact solution of the standard NLS equation [10]. In this regard, one can extract the ideal initial states from our analytic results for different types of optical excitations. On the other hand, in recent work [49] the stability of the multipeak solitons and other nonlinear waves in the femtosecond regime has been confirmed by numerical simulations. Thus, our results

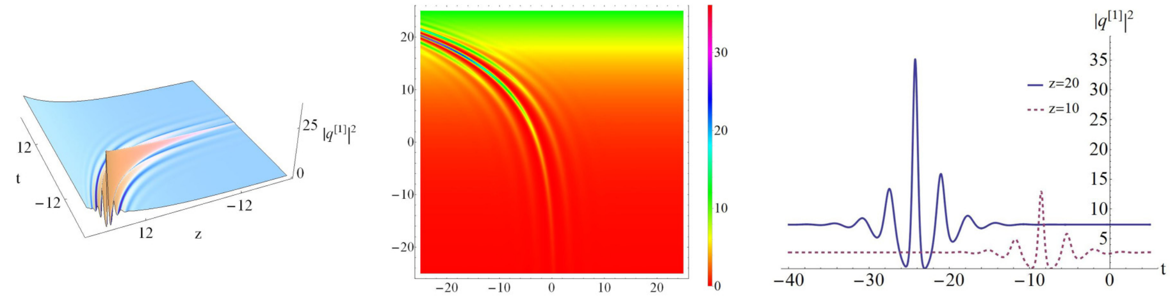

(a) (b) (c)

FIG. 8. The effect of gain and loss coefficient on the multipeak solitons with $\delta_1 = \delta_3 = 0.1$, $\xi = 0.1$, $k_1 = k_2 = 1$, and $\lambda_1 = \lambda_2^* = 0.2 + 0.6\,i$. (b) is the density plot of (a). (c) is the cross-sectional view of (a) at $z = 10$ and $z = 20$.

could offer the possibility to realize rich nonlinear structures experimentally in the femtosecond regime of a fiber.

III. MI CHARACTERISTICS

In this section, we reveal the explicit relation between the transition and the distribution characteristics of MI growth rate for Eq. (1). Equation (1) admits the following continuous wave solution,

$$q(z,t) = c(z)\,e^{i\,[m(z)+n\,t]} = \sqrt{\frac{d_2(z)}{R(z)}}\,e^{i\,[m(z)+n\,t]}, \tag{15}$$

where n are real parameters. A perturbed nonlinear background can be expressed as

$$q(z,t) = [c(z) + \epsilon\,\widehat{q}(z,t)]\,e^{i\,[m(z)+n\,t]}. \tag{16}$$

Taking Eq. (16) into Eq. (1) yields the evolution equation for the perturbations as

$$\begin{aligned}&-i\,R(z)\,\widehat{q}\,d_2(z)_z + d_2(z)^2R(z)(2\,\widehat{q} + 2\,\widehat{q}^* + 2\,i\,n\,\widehat{q}_t + \widehat{q}_{tt})\\&\quad + d_2(z)(2\,d_3(z)R(z)(6\,n\,\widehat{q} + 6\,n\,\widehat{q}^* - 6\,i\,\widehat{q}_t + 3\,i\,n^2\widehat{q}_t\\&\quad + 3\,n\,\widehat{q}_{tt} - i\,\widehat{q}_{ttt}) + i\,[\widehat{q}\,R(z)_z + 2R(z)\widehat{q}_z]) = 0.\end{aligned} \tag{17}$$

Noting the linearity of Eq. (17) with respect to $\widehat{q}$, we introduce

$$\widehat{q}(z,t) = u\,c(z)\,e^{i\,[Q\,t-\omega(z)]} + v\,c(z)\,e^{-i\,[Q\,t-\omega^*(z)]}, \tag{18}$$

which is characterized by the wave number ω and frequency Q. Using Eq. (18) into Eq. (17) gives a linear homogeneous system of equations for u and v:

$$\begin{aligned}&d_2(z) - n\,Q\,d_2(z) - \tfrac{1}{2}Q^2\,d_2(z) + 6\,n\,d_3(z) + 6\,Q\,d_3(z)\\&\quad -3\,n^2\,Q\,d_3(z) - 3\,n\,Q^2\,d_3(z) - Q^3\,d_3(z) + \omega_z(z) = 0,\end{aligned} \tag{19}$$

$$d_2(z) + 6\,n\,d_3(z) = 0. \tag{20}$$

From the determinant of the coefficient matrix of Eqs. (19)–(20), the dispersion relation for the linearized disturbance can be determined as

$$\begin{aligned}&n\,Qd_2(z)[d_3(z)(Q^3 - 6n^2Q) + 2\omega_z(z)]\\&\quad + 2Qd_3(z)(3n^2 + Q^2 - 6)\omega_z(z)\\&\quad + \tfrac{1}{4}Q^2d_2(z)^2(-4n^2 + Q^2 - 4) - Q^2d_3(z)^2(9n^4\\&\quad -3n^2Q^2 + (Q^2 - 6)^2) - \omega_z(z)^2 = 0.\end{aligned} \tag{21}$$

Solving the above equation, we have

$$\begin{aligned}\omega(z) = {}& Q\,(d_2(z)\,n + d_3(z)(-6 + 3\,n^2 + Q^2))\\&\pm\tfrac{1}{2}|Q|\sqrt{[d_2(z) + 6\,d_3(z)\,n]^2\,(-4 + Q^2)}.\end{aligned} \tag{22}$$

In this case, the wave number $\omega(z)$ becomes complex and the disturbance will grow with time exponentially if and only if $Q < Q_c = 2$, and the growth rate of the instability is given by

$$\Omega(z) = \frac{1}{2}Q^2\sqrt{[d_2(z) + 6\,d_3(z)\,n]^2\left(\frac{4}{Q^2} - 1\right)}. \tag{23}$$

To obtain the maximum growth rate of the instability, we take the derivative of Eq. (23) with respect to Q, and set it to zero. Then, we obtain $Q_{\max} = \sqrt{2}$ and the following maximum growth rate of the instability:

$$\Omega(z)_{\max} = \sqrt{[d_2(z) + 6\,d_3(z)\,n]^2}. \tag{24}$$

The effects of the TOD coefficient on the growth rate of instability is demonstrated in Fig. 10, from which we discover that the value of $\Omega(z)$ increases with the value of $d_3(z)$. Figure 11 shows the characteristics of MI on the (Q,n) plane. It is found that the MI exists in the region $-2 < Q < 2$. Hereby, we discover that the MI growth rate distribution is symmetric

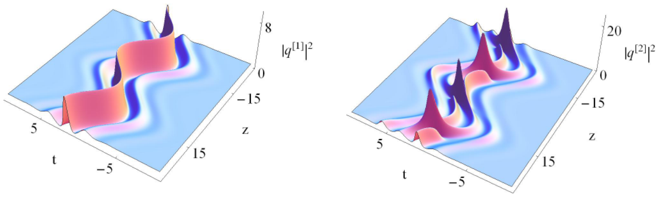

(a) (b)

FIG. 9. Periodic variable motion of the multipeak solitons with $\delta_1 = \delta_2 = \delta_3 = 0.1$, $\xi = 0.2$, (a) The first-order multipeak soliton with $k_1 = 1$, $k_2 = -1$, $\lambda_1 = \lambda_2^* = 0.3 + 0.7\,i$. (b) The periodic collision between two multipeak solitons with $k_1 = 1$, $k_2 = -1$, $\lambda_1 = \lambda_2^* = 0.3 + i$, $\lambda_3 = \lambda_4^* = 0.3 + 0.8\,i$.

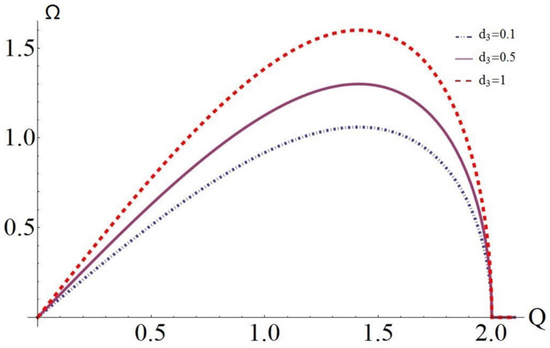

FIG. 10. The effects of d_3 on the growth rate of instability with $n = 0.1, d_2 = 1$.

with respect to

$$n = -\frac{d_2(z)}{6\,d_3(z)}, \tag{25}$$

i.e., The red dashed line in Fig. 11 corresponds to a modulational stability (MS) region where the growth rate is vanishing in the low perturbation frequency region. More interestingly, using the rogue-wave eigenvalue, one can find that the MS condition (25) is consistent with the condition (5), which converts breathers into nonlinear waves on constant backgrounds. Our finding suggests that the transition between breathers and nonlinear waves can occur in the MS region with the low-frequency perturbations. Further, by comparison with Fig. 11(a), we discover that the lower value of $d_3(z)$ corresponds to the lower value of n. Therefore, the MS region moves down, which is displayed in Fig. 11(b).

IV. BREATHER MULTIPLE BIRTHS AND PEREGRINE COMBS AND WALLS

In this section, we will study the breather solution (3) in detail, and describe its main properties when the GVD coefficient is of the form

$$d_2(z) = c\,R(z) = -1 + d_c\,\cos(k_c\,z), \tag{26}$$

where d_c denotes the amplitude of modulation and k_c is spatial frequency. Such periodic modulations have realized experimentally in Ref. [50].

The spatiotemporal characteristics of the breather multiple births described by the solution (3) are illustrated in Fig. 12, i.e., the triplets structure with $d_c = 2.5$ and the septuplets structure with $d_c = 8.5$. These structures show multiple compression points, located at different values of z and t. The number of the ABs in the breather multiple births depends on the amplitude of the modulation but not on its wavelength, which controls their separation distance. Increasing the value of d_c will lead to the formation of $(3+4k)$ births for $k = 2,3,\ldots$. With the similar modulation parameters selected, these multiple births structures have been also reported in the vc-NLS equation, the vc-DNLS equation, and the vc-NLS-MB system. The difference is, however, that the phase shifts of the ABs on the sides of the center occur along t direction because of the TOD effect [for example, see Fig. 12(a)], which don't exist in the vc-NLS equation without higher-order effect.

If $\lambda = \alpha + \beta\,i \rightarrow -\frac{n}{2} + i$, we can obtain another type of multiple compression point structure, namely the Peregrine combs that are the limiting case of the breather multiple births. The Peregrine comb solution can be given by

$$q_{\text{comb}}(z,t) = e^{i\rho}\left(c(z) - 2\frac{(i+2\,Z_c)^2 + 4\,M^2}{1 + 4\,Z_c^2 + 4\,M^2}\right), \tag{27}$$

with

$$Z_c = -z + \frac{d_c}{k_c}\sin(k_c\,z), \quad M = t + 6\,z\,d_3(z).$$

From the above expression, we see that the Peregrine comb solution (27) includes the gain or loss $\Gamma(z)$ that controls the amplitude, and TOD coefficient $d_3(z)$ that affect the spatial-temporal distribution. The Peregrine combs were first found in the vc-NLS equation [23], and then were also found in the vc-coupled Hirota equations [43]. These phenomena do not take place in the standard AB or PS without variable dispersion, which contain only one compression point. The maximum value of this wave's amplitude is obtained at $t = -6\,d_3(z)z$

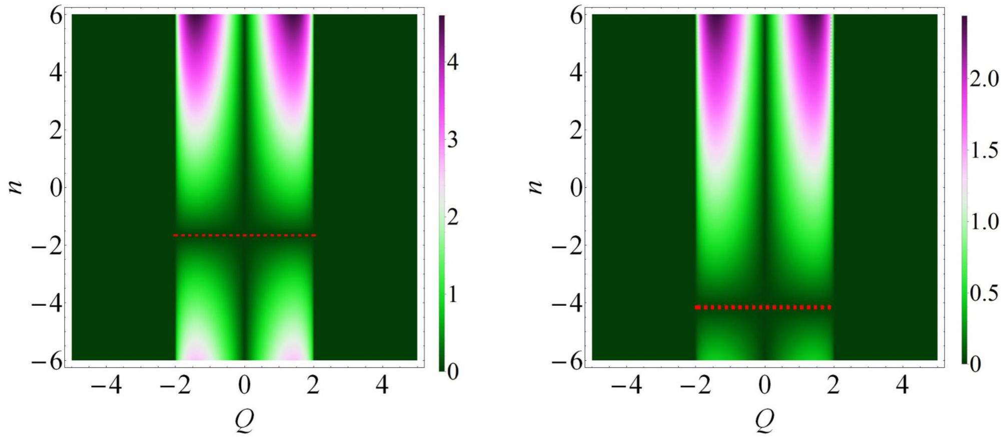

(a) (b)

FIG. 11. Characteristics of MI growth rate ω on (Q,n) plane with $d_2(z) = 1$ and $(a) d_3(z) = 0.1$; $(b) d_3(z) = 0.04$. Here the dashed red lines represent the stability region in the perturbation frequency region $-2 < Q < 2$, which is given as $n = -\frac{d_2(z)}{6\,d_3(z)}$.

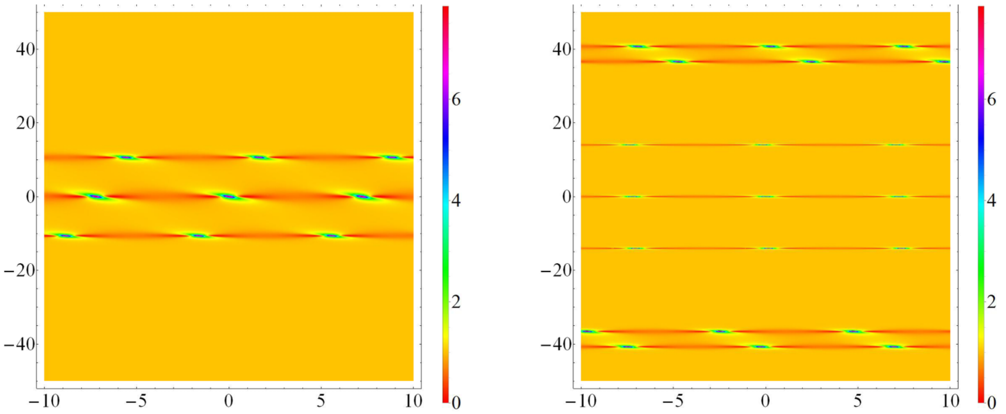

(a) (b)

FIG. 12. The breather multiple births with $R(z) = d_2(z)$, $k_c = 0.2$, $d_3(z) = 0.1$, $n = 0$, $k_1 = 1$, $k_2 = -1$, $\lambda_1 = \lambda_2^* = 0.9\,i$, and (a) three births with $d_c = 2.5$, (b) seven births with $d_c = 8.5$.

and is given as follows:

$$\begin{aligned}|q_{\text{comb}}|^2_{\max}(z) &= |q_{\text{comb}}[z, -6\,d_3(z)z]|^2\\ &= \frac{(1-4\,Z_c^2)4\,c(z)}{1+4\,Z_c^2} + c(z)^2 + 4,\end{aligned} \tag{28}$$

with

$$Z_c = -z\left[1 - \frac{d_c}{k_c\,z}\sin(k_c\,z)\right]. \tag{29}$$

The GVD coefficient $d_2(z)$ or TOD coefficient $d_3(z)$ has no effect on the maximum intensity of the Peregrine comb, which is related to the gain or loss coefficient $\Gamma(z)$. From the equation (28), we find that $|q_{\text{comb}}|^2_{\max}(z)$ reaches its maximal value $[c(z)+2]^2$ at $Z_c = 0$. This means that the compression points of the Peregrine comb are located at $z_0 = 0$, z_i ($i = 1,2,\ldots$), where z_i satisfy the following equation

$$\frac{\sin(k_c z_i)}{k_c z_i} = \frac{1}{d_c}. \tag{30}$$

Equation (30) shows that the larger the value of d_c is, the more compression points will be. For example, Fig. 13(a) displays a Peregrine comb with triple teeth of Eq. (1) with $d_c = 2.5$, and Fig. 13(c) is plotted for a Peregrine comb with seven teeth with $d_c = 8.5$. The detailed generation process of Peregrine combs with seven teeth can refer to the explanations for the vc-NLS equation in Ref. [23].

In order to explore the dynamics of the Peregrine comb, we calculate some physical quantities of the Peregrine comb analytically. The maximum points, intersection angle θ and the distance between A and B can be presented as follows

$$(0,0),\quad \left(-\frac{\arccos\left(\frac{1}{d_c}\right)}{k_c}, \frac{6\,d_3(z)\arccos\left(\frac{1}{d_c}\right)}{k_c}\right),$$
$$\left(\frac{\arccos\left(\frac{1}{d_c}\right)}{k_c}, -\frac{6\,d_3(z)\arccos\left(\frac{1}{d_c}\right)}{k_c}\right), \tag{31}$$

$$\theta = \arctan\left(-\frac{1}{6\,d_3(z)}\right), \tag{32}$$

$$D_{AB} = \sqrt{1+36\,d_3^2(z)}\frac{\arccos\left(\frac{1}{d_c}\right)}{k_c}. \tag{33}$$

Bases on the above analytic expressions, we find that the TOD effect $d_3(z)$ plays an important role in the spatiotemporal characteristics of the Peregrine comb. Increasing the values of $d_3(z)$ will increase the distance between A and B while decrease the intersection angle θ, which is shown in Fig. 14.

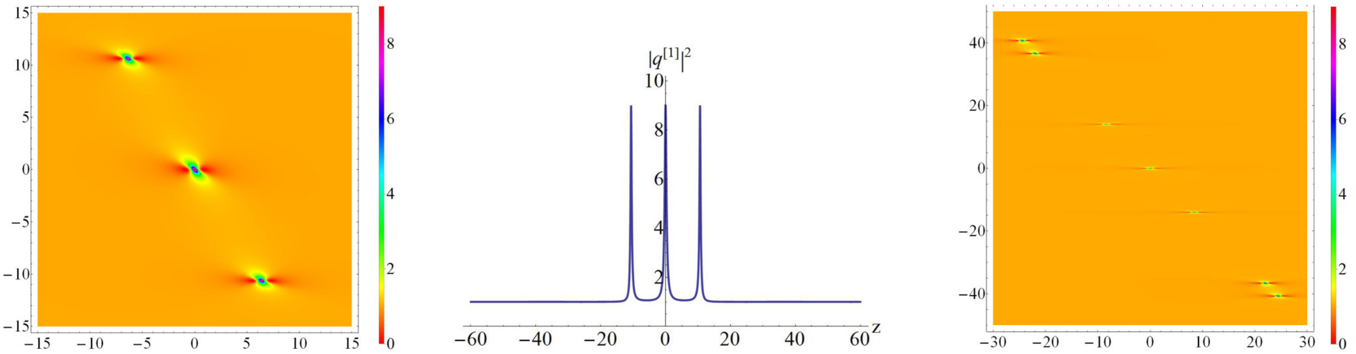

(a) (b) (c)

FIG. 13. The Peregrine combs with $R(z) = d_2(z)$, $k_c = 0.2$, $d_3(z) = 0.1$, $n = 0$, $k_1 = 1$, $k_2 = -1$, $\lambda_1 = \lambda_2^* = -\frac{n}{2} + i$, and (a) triple teeth with $d_c = 2.5$, (b) the cross-sectional view of (a) along $t = -6\,d_3(z)z$. (c) seven teeth with $d_c = 8.5$.

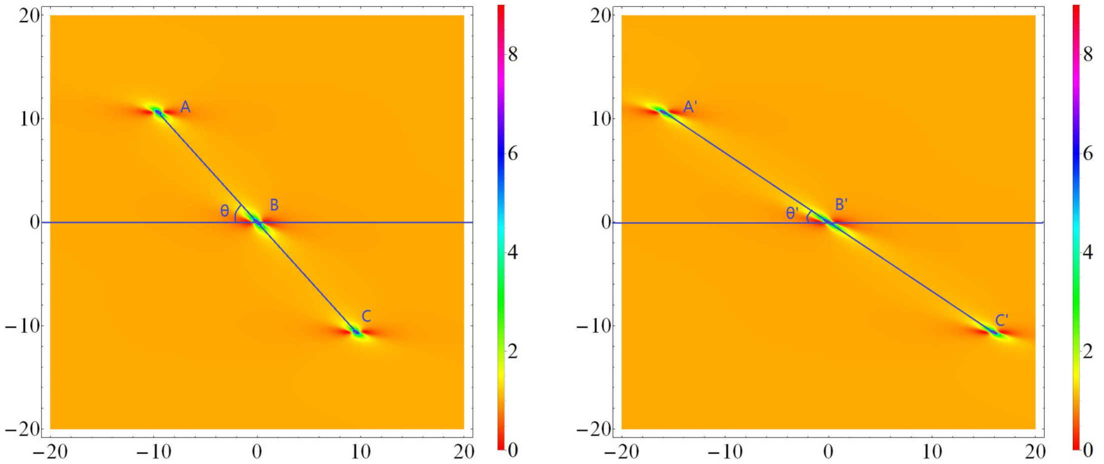

(a) (b)

FIG. 14. The effect of d_3 on the Peregrine comb with $R(z) = d_2(z)$, $d_c = 2.5$, $k_c = 0.2$, $n = 0$, $k_1 = k_2 = 1$, $\lambda_1 = \lambda_2^* = -\frac{n}{2} + i$, and (a) $d_3(z) = 0.15$, (b) $d_3(z) = 0.25$.

If $d_3(z)$ is equal to zero, the Peregrine comb in Fig. 14 will degenerate into the case in Ref. [23].

In order to reveal further characteristics of the Peregrine comb, we introduce the energy of light pulse against the plane-wave background with the form [23,28,51]

$$\begin{aligned}\Delta I_c(z,t) &= |q_{PS}(z,t)|^2 - c(z)^2 \\ &= 4\frac{F_+ F_- - c(z) K_+ K_-}{\{1 + 4Z^2 + 4[t + 6z\, d_3(z)]^2\}^2},\end{aligned} \tag{34}$$

with

$$\begin{aligned}F_- &= 4t^2 + 4Z^2 + [1 - 12z\, d_3(z)]^2 + t[-4 + 48z\, d_3(z)], \\ F_+ &= 4t^2 + 4Z^2 + [1 + 12z\, d_3(z)]^2 + t[4 + 48z\, d_3(z)], \\ K_- &= -1 + 4Z^2 + 4[t + 6z\, d_3(z)]^2, \\ K_+ &= 1 + 4Z^2 + 4[t + 6z\, d_3(z)]^2.\end{aligned} \tag{35}$$

One can easily check

$$\int_{-\infty}^{\infty} \Delta I_c(z,t) dt = 0, \tag{36}$$

for all values of z. This implies that the energy of the pump is preserved along the fiber, in spite of periodic modulation characteristics and TOD effect added. In addition, Eq. (35) also reflects the fact that the light intensity of the Peregrine comb will be sometimes higher and sometimes lower than the background intensity, as shown in Fig. 15. Moreover, we can calculate the energy of the Peregrine pulse

$$\begin{aligned}E_{\text{pluse}}(z) &= \int_{-\infty}^{\infty} |q_{\text{comb}}(t,z) - q_{\text{comb}}(\pm\infty,z)|^2 dt \\ &= \frac{4\pi}{\sqrt{1+4Z_c^2}},\end{aligned} \tag{37}$$

which indicates that the energy of the pulse is maximal at the compression points $Z_c = 0$ (also see Fig. 16).

Next, we consider another special case of the generalized PS solution, namely the Peregrine walls. From the equation (31), we note that the amplitude of modulation d_c and spatial frequency k_c also affect the positions of two of maximum points, i.e., $(\mp\frac{\arccos(\frac{1}{d_c})}{k_c}, \pm\frac{6\, d_3(z) \arccos(\frac{1}{d_c})}{k_c})$. In particular, we consider a special case in which the amplitude of modulation d_c is set to be 1. This will result in the case $\arccos(\frac{1}{d_c}) = 0$. Thus, these two maximum points will be shifted to the origin and these three PSs will be aggregated together. In this case,

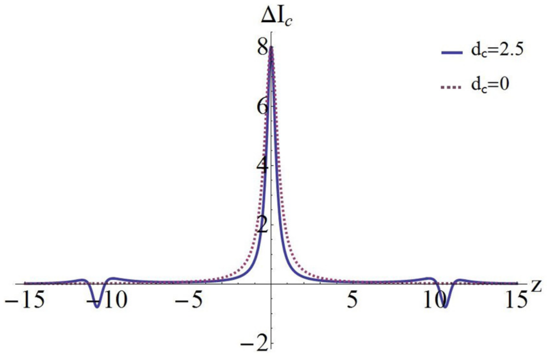

FIG. 15. The distribution of the difference between the light intensities of the PS and the CW background at $t = 0$ given by Eq. (34) with $k_c = 0.2$, $d_3 = 0.02$, $d_c = 0$ (dashed line), and $d_c = 2.5$ (solid line).

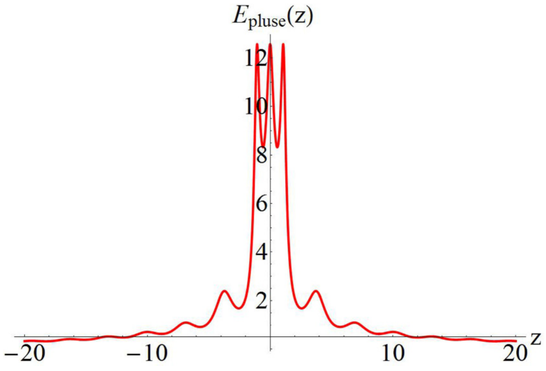

FIG. 16. Pulse energy $E_{pulse}(z)$ with $k_c = 2$, $d_c = 2.5$.

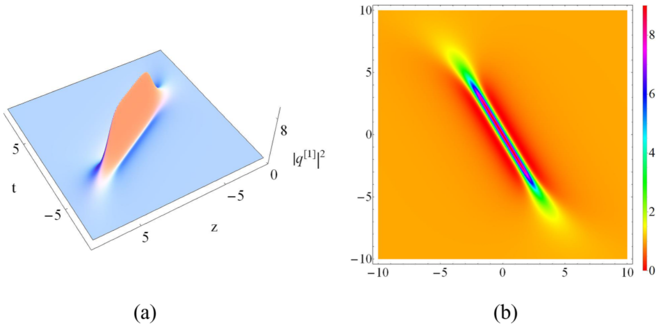

FIG. 17. The Peregrine wall with $R(z) = d_2(z)$, $k_c = 0.2$, $d_3(z) = 0.1$, $n = 0$, $k_1 = 1$, $k_2 = -1$, $\lambda_1 = \lambda_2^* = -\frac{n}{2} + i$, and $d_c = 1$. (b) is the density plot of (a).

the Peregrine comb solution (27) turns into the form of

$$|q_{\mathrm{wall}}(z,t)|^2 = [c(z) - 2]^2 + \frac{M\,(8 + 9\,M)}{W^2} + \frac{2\,[-6\,M + (4 + 3\,M)c(z)]}{W}, \qquad (38)$$

with

$$W = (1 + M + 4\,z^2) + 4\frac{\sin(k_c z)}{k_c^2}[\sin(k_c z) - 2\,k_c z].$$

The maximum value of this wave's amplitude is obtained at $t = -6\,d_3(z)z$ and is given by

$$|q_{\mathrm{wall}}|^2_{\max}(z) = |q_{\mathrm{wall}}[z, -6\,d_3(z)z]|^2 = [c(z) - 2]^2 + \frac{8\,c(z)}{W_0}, \qquad (39)$$

with

$$W_0 = (1 + 4\,z^2) + 4\frac{\sin(k_c z)}{k_c^2}[\sin(k_c z) - 2\,k_c z].$$

As depicted in Fig. 17, the Peregrine comb is converted into a Peregrine wall when the three maximum points have the same coordinate (0,0). Generally, the fusion of three PSs will produce a second-order rogue wave with higher amplitude in the nonlinear equation of evolutions with constant coefficients. However, the variable coefficients provide much richer patterns. The Peregrine wall can be seen as an intermediate state between the rogue wave and W-shaped soliton because rogue wave has a shorter life while W-shaped soliton has a long one. Such structure looks like a quasitrapezoid in shape. The values of the hump and valleys of the Peregrine wall, respectively, are equal to $[c(z) + 2]^2$ and 0. To illustrate the effect of TOD coefficient on the Peregrine wall, we plot Fig. 18. It is observed that the length of the wave increases with growing value of $d_3(z)$, and the depth and angle decreases. In fact, similar to the Peregrine comb, the Peregrine wall can also be viewed as the limiting case of a breath-type wall that is described in Fig. 19. On the other hand, to illustrate how to build a Peregrine wall from a PS, we plot Fig. 20 with different values of d_c. As d_c increases, the lifetime of the PS gets much longer. When d_c is equal to 1, the PS eventually becomes a Peregrine wall. When d_c is greater than 1, the PS will show multiple compression points, i.e., it turns into the Peregrine comb [23].

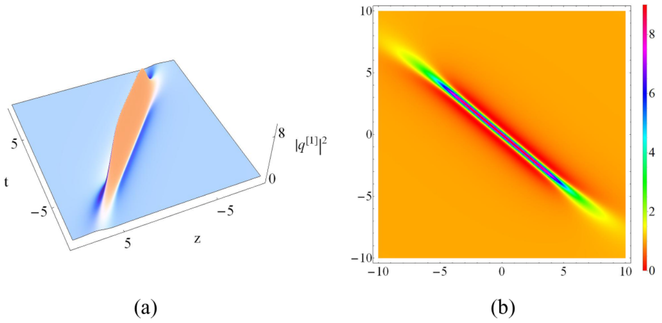

FIG. 18. The effect of $d_3(z)$ on the Peregrine wall with $R(z) = d_2(z)$, $k_c = 0.2$, $d_3(z) = 0.2$, $n = 0$, $k_1 = 1$, $k_2 = -1$, $\lambda_1 = \lambda_2^* = -\frac{n}{2} + i$, and $d_c = 1$. (b) is the density plot of (a).

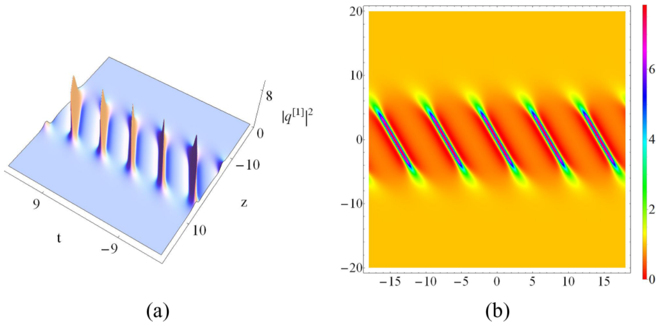

FIG. 19. The breath-type wall with $R(z) = d_2(z)$, $k_c = 0.2$, $d_3(z) = 0.1$, $n = 0$, $k_1 = 1$, $k_2 = -1$, $\lambda_1 = \lambda_2^* = -\frac{n}{2} + 0.9\,i$, and $d_c = 1$. (b) is a density plot of (a).

The frequency spectrum of the Peregrine comb in Eq. (27) can be given by

$$\begin{aligned} F(\omega,z) &= \frac{1}{\sqrt{2\pi}} \int_{-\infty}^{\infty} q_{\mathrm{comb}}(z,t) e^{i\,\omega\,t} dt \\ &= \sqrt{2\pi}\left(\frac{1 - 2\,i\,Z_c}{\sqrt{1 + 4\,Z_c^2}} e^{-\frac{i\,|\omega|}{2}(12\,d_3(z)\,z + \sqrt{-1-4Z_c^2})} - \delta(\omega)\right), \end{aligned} \qquad (40)$$

where the Dirac delta function $\delta(\omega)$ originates from the finite background level. The modulus of this spectrum is

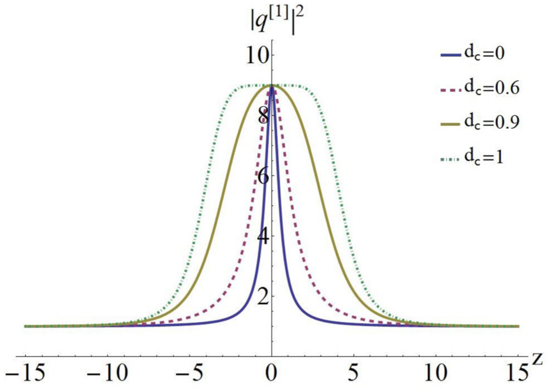

FIG. 20. Graph of $|q_{\mathrm{wall}}(z, -6\,d_3(z)z)|^2$ for value of d_c with $k_c = 0.2$, $d_3 = 0.1$ shows the evolution process from rogue wave to the comb.

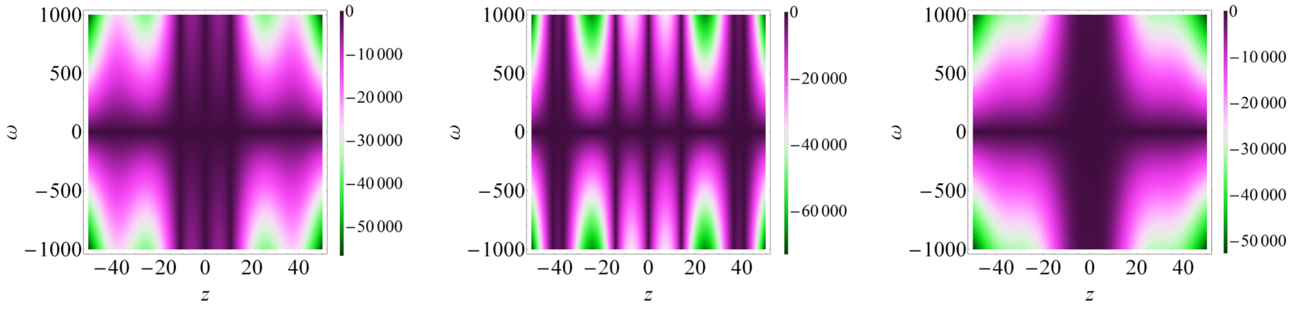

(a) (b) (c)

FIG. 21. The spectrum of the Peregrine combs and Peregrine wall log scale, namely, $\log|F(w,z)|$ $k_c = 0.2$, $d_3(z) = 0.1$ and (a) for the triple-tooth comb with $d_c = 2.5$, (b) for the seven-tooth comb with $d_c = 8.5$, and (c) for the Peregrine wall with $d_c = 1$.

given by

$$|F(\omega,z)| = \sqrt{2\pi}\, e^{-\frac{|\omega|}{2}\sqrt{1+4\,Z_c^2}}. \tag{41}$$

It is well known that the Peregrine rogue-wave spectrum features a triangular shape and gets dramatically broadened at the maximally compressed peak. To end this section, we consider the spectral property of the Peregrine combs and Peregrine walls. From Fig. 21(a), we observe that the rogue wave in Eq. (1) begins with narrow spectral components as the constant-coefficient ones, but spreads and shrinks during the evolution along the fiber, and eventually restores its initial shape. Each nonlinear spreading in the spectrum is related to a corresponding maximal compression point. Therefore, the number of spectral components increases with the amplitude of modulation, which is displayed in Fig. 21(b). Figure 21(c) shows the spectrum of the Peregrine wall. It is observed that the width of nonlinear spreading are obviously greater than that of the Peregrine comb.

Finally, we discuss the possible applications of the Peregrine combs and Peregrine walls. As is well-known, the vc-NLS equations provide more realistic models than their constant coefficient counterparts, although they have analytical solutions only if the integrability condition is satisfied. In particular, Tiofack *et al.* showed recently that the spatiotemporal evolution of the generalized Peregrine solution in the nonintegrable case and observed that there still are multiple compression points [23], which agrees with theoretical prediction. Further, they have chosen for SPM and Kerr nonlinear effect values corresponding to those of an experimentally realizable photonic crystal fiber with a GVD and nonlinear coefficients that are periodically modulated along the physical propagation axis z' and the real time T. By using the corresponding characteristics of the photonic crystal fiber, the periodic evolution of the GVD and the nonlinear coefficient versus the longitudinal z' axis was calculated at the pump wavelength $\lambda_p = 1700$ nm and pump power $P_0 = 1.7$ W [23]. They thus use the above results, and then integrate numerically a vc-NLS equation with the initial condition given by the Peregrine comb solution with $z_0 = 1.25$, expressed in the original physical variables given in Ref. [23]. Their result indicates that the solution still produces multiple compression points. These studies show that the generalized PS solution is a robust one that persists in cases where the integrability condition is destroyed or the realizable optical application is considered. As the RWs and breathers reported experimentally, we expect that the Peregrine combs and Peregrine walls could be observed in nonlinear fibers with periodically modulated characteristics in the future.

V. CONCLUSIONS

We have carried out the analytical investigations on the vc-NLS equation with higher-order effects. It has been shown that the breather solution can be converted into the multipeak solitons (single and double main peaks), antidark soliton, periodic wave, and W-shaped soliton. The transition condition depending on the eigenvalue, GVD coefficient, and TOD coefficient has been given analytically. We have demonstrated that different types of nonlinear waves can coexist and interact with each other elastically. We have further revealed the effects of the variable coefficients on the multipeak solitons: (i) The GVD coefficient controls the number of peaks of the wave; (ii) The TOD coefficient accounts for the compressed effects of the wave (the location of the wave); (iii) The gain or loss coefficient is responsible for the amplitude of the wave. The transition between breathers and nonlinear waves occurs in the MS region with the low-frequency perturbations. We have shown that, under the suitable periodic modulations, the Peregrine combs ($d_c > 1$) and Peregrine walls ($d_c = 1$) are formed. We have discovered that the TOD coefficient has influence on the spatiotemporal characteristics of the Peregrine combs and Peregrine walls. Our results could provide certain theoretical assistance to the experimental control and manipulation of generalized rogue wave dynamics in inhomogeneous fiber.

ACKNOWLEDGMENTS

We express our sincere thanks to all the members of our discussion group for their valuable comments. This work has been supported by the National Natural Science Foundation of China under Grants No. 11305060 and No. 61505054, by the Fundamental Research Funds of the Central Universities (No. 2015ZD16), and by the Innovative Talents Scheme of North China Electric Power University.

APPENDIX

With the Ablowitz-Kaup-Newell-Segur formalism, the Lax pair associated with Eq. (1) can be written as [40]

$$\Phi_t = U\,\Phi, \quad \Phi_z = V\,\Phi, \tag{A1}$$

where U and V are

$$\Phi = \begin{pmatrix} \varphi \\ \psi \end{pmatrix}, \quad U = -i\,\lambda\, J + \sqrt{\frac{R(z)}{d_2(z)}}\,\Lambda \quad V = i\,4\,d_3(z)\lambda^3 J - i\,\lambda^2 d_2(z)\,J - 4\lambda^2\,d_3(z)\sqrt{\frac{R(z)}{d_2(z)}}\,\Lambda + \lambda\,R + \frac{i}{2}\,Q \tag{A2}$$

with

$$J = \begin{pmatrix} 1 & 0 \\ 0 & -1 \end{pmatrix}, \quad \Lambda = \begin{pmatrix} 0 & q \\ -q^* & 0 \end{pmatrix},$$

$$R = \begin{pmatrix} R_{11} & R_{12} \\ R_{21} & R_{22} \end{pmatrix}, \quad R_{11} = \frac{-2\,i\,d_3(z)|q|^2 R(z)}{d_2(z)}, \quad R_{12} = \sqrt{\frac{R(z)}{d_2(z)}}\left[d_2(z)q - 2\,i\,d_3(z)\frac{\partial q}{\partial t}\right],$$

$$R_{21} = -\sqrt{\frac{R(z)}{d_2(z)}}\left[d_2(z)q^* + 2\,i\,d_3(z)\frac{\partial q^*}{\partial t}\right], \quad R_{22} = \frac{2\,i\,d_3(z)|q|^2 R(z)}{d_2(z)},$$

$$Q = \begin{pmatrix} Q_{11} & Q_{12} \\ Q_{21} & Q_{22} \end{pmatrix}, \quad Q_{11} = R(z)|q|^2 - \frac{i\,d_3(z)R(z)}{d_2(z)}\left(2\,q^*\frac{\partial q}{\partial t} - 2q\frac{\partial q^*}{\partial t}\right),$$

$$Q_{12} = \sqrt{\frac{R(z)}{d_2(z)}}\left[d_2(z)\frac{\partial q}{\partial t} - 2\,i\,d_3(z)\left(\frac{2\,q\,|q|^2 R(z)}{d_2(z)} + \frac{\partial^2 q}{\partial t^2}\right)\right],$$

$$Q_{21} = \sqrt{\frac{R(z)}{d_2(z)}}\left[d_2(z)\frac{\partial q^*}{\partial t} + 2\,i\,d_3(z)\left(\frac{2\,q^*\,|q|^2 R(z)}{d_2(z)} + \frac{\partial^2 q^*}{\partial t^2}\right)\right],$$

$$Q_{22} = -R(z)|q|^2 + \frac{i\,d_3(z)R(z)}{d_2(z)}\left(2\,q^*\frac{\partial q}{\partial t} - 2q\frac{\partial q^*}{\partial t}\right),$$

λ is the spectral parameter and Φ is the eigenfunction. Through direct computations, it can be verified that the equation $U_z - V_t + [U,V] = 0$ exactly yields Eq. (1).

By using the transformation $\Phi^{[n]} = T\,\Phi$, we obtain the new Lax pair $\Phi_t^{[n]} = U^{[n]}\,\Phi^{[n]}$, $U^{[n]} = (T_t + T\,U)T^{-1}$, $\Phi_z^{[n]} = V^{[n]}\,\Phi^{[n]}$, $V^{[n]} = (T_z + T\,V)T^{-1}$, where T is a 2×2 matrix determined by the above relations $U_z^{[n]} - V_t^{[n]} + [U^{[n]},V^{[n]}] = T(U_z - V_t + [U,V])T^{-1}$.

This implies that, in order to keep the Lax pair (A1) invariant under the transformation, it is crucial to seek a matrix T such that $U^{[n]}$ and $V^{[n]}$ have the same forms as those of U and V. In addition, the old potentials q are mapped into new ones $q^{[n]}$.

Next, we shall construct the n-fold Darboux transformation of Eq. (1). Hereby, we assume Matrix T_n be the form of

$$T_n = T_n(\lambda;\lambda_1,\lambda_2,\ldots,\lambda_{2n}) = \sum_{l=0}^{n} M_l\,\lambda^{n-l}, \tag{A3}$$

where Matrices M_l $(l = 0,1,2,\ldots,n-1)$ are solved by Cramer's rule, $\lambda_k = \alpha_k + i\,\beta$ $(k = 1,2,\ldots,2n)$ denote the spectral parameters and M_n is an identity matrix.

Solving the linear system

$$\begin{aligned}\Phi_k^{[n]} &= T_n(\lambda;\lambda_1,\lambda_2,\ldots,\lambda_{2n-1},\lambda_{2n})|_{\lambda=\lambda_k}\Phi_k \\ &= \sum_{l=0}^{n} M_l\,\lambda_k^{n-l}\,\Phi_k = 0 \quad (k = 1,2,\ldots,2n),\end{aligned} \tag{A4}$$

where $\Phi_k = (\varphi_k,\psi_k)^T$ are the solutions of Lax pair (A1), we can get the determinant representation of the T_n as follows:

$$T_n = T_n(\lambda;\lambda_1,\lambda_2,\ldots,\lambda_{2n}) = \begin{pmatrix} \frac{(\Omega_n)_{11}}{\Delta_n} & \frac{(\Omega_n)_{12}}{\Delta_n} \\ \frac{(\Omega_n)_{21}}{\Delta_n} & \frac{(\Omega_n)_{22}}{\Delta_n} \end{pmatrix}, \tag{A5}$$

with

$$\Delta_n = \begin{vmatrix} \varphi_1 & \psi_1 & \cdots & \lambda_1^{n-2}\varphi_1 & \lambda_1^{n-2}\psi_1 & \lambda_1^{n-1}\varphi_1 & \lambda_1^{n-1}\psi_1 \\ \varphi_2 & \psi_2 & \cdots & \lambda_2^{n-2}\varphi_2 & \lambda_2^{n-2}\psi_2 & \lambda_2^{n-1}\varphi_2 & \lambda_2^{n-1}\psi_2 \\ \vdots & \vdots & \vdots & \vdots & \vdots & \vdots & \vdots \\ \varphi_{2n} & \psi_{2n} & \cdots & \lambda_{2n}^{n-2}\varphi_{2n} & \lambda_{2n}^{n-2}\psi_{2n} & \lambda_{2n}^{n-1}\varphi_{2n} & \lambda_{2n}^{n-1}\psi_{2n} \end{vmatrix},$$

$$(\Omega_n)_{11} = \begin{vmatrix} 1 & 0 & \lambda & 0 & \cdots & \lambda^{n-1} & 0 & \lambda^n \\ \varphi_1 & \psi_1 & \lambda_1\varphi_1 & \lambda_1\psi_1 & \cdots & \lambda_1^{n-1}\varphi_1 & \lambda_1^{n-1}\psi_1 & \lambda_1^n\varphi_1 \\ \varphi_2 & \psi_2 & \lambda_2\varphi_2 & \lambda_2\psi_2 & \cdots & \lambda_2^{n-1}\varphi_2 & \lambda_2^{n-1}\psi_2 & \lambda_2^n\varphi_2 \\ \vdots & \vdots & \vdots & \vdots & \vdots & \vdots & \vdots & \vdots \\ \varphi_{2n} & \psi_{2n} & \lambda_{2n}\varphi_{2n} & \lambda_{2n}\psi_{2n} & \cdots & \lambda_{2n}^{n-1}\varphi_{2n} & \lambda_{2n}^{n-1}\psi_{2n} & \lambda_{2n}^n\varphi_{2n} \end{vmatrix},$$

$$(\Omega_n)_{12}=\begin{vmatrix} 0 & 1 & 0 & \lambda & \cdots & 0 & \lambda^{n-1} & 0 \\ \varphi_1 & \psi_1 & \lambda_1\varphi_1 & \lambda_1\psi_1 & \cdots & \lambda_1^{n-1}\varphi_1 & \lambda_1^{n-1}\psi_1 & \lambda_1^{n}\varphi_1 \\ \varphi_2 & \psi_2 & \lambda_2\varphi_2 & \lambda_2\psi_2 & \cdots & \lambda_2^{n-1}\varphi_2 & \lambda_2^{n-1}\psi_2 & \lambda_2^{n}\varphi_2 \\ \vdots & \vdots & \vdots & \vdots & \vdots & \vdots & \vdots & \vdots \\ \varphi_{2n} & \psi_{2n} & \lambda_{2n}\varphi_{2n} & \lambda_{2n}\psi_{2n} & \cdots & \lambda_{2n}^{n-1}\varphi_{2n} & \lambda_{2n}^{n-1}\psi_{2n} & \lambda_{2n}^{n}\varphi_{2n} \end{vmatrix},$$

$$(\Omega_n)_{21}=\begin{vmatrix} 1 & 0 & \lambda & 0 & \cdots & \lambda^{n-1} & 0 & 0 \\ \varphi_1 & \psi_1 & \lambda_1\varphi_1 & \lambda_1\psi_1 & \cdots & \lambda_1^{n-1}\varphi_1 & \lambda_1^{n-1}\psi_1 & \lambda_1^{n}\psi_1 \\ \varphi_2 & \psi_2 & \lambda_2\varphi_2 & \lambda_2\psi_2 & \cdots & \lambda_2^{n-1}\varphi_2 & \lambda_2^{n-1}\psi_2 & \lambda_2^{n}\psi_2 \\ \vdots & \vdots & \vdots & \vdots & \vdots & \vdots & \vdots & \vdots \\ \varphi_{2n} & \psi_{2n} & \lambda_{2n}\varphi_{2n} & \lambda_{2n}\psi_{2n} & \cdots & \lambda_{2n}^{n-1}\varphi_{2n} & \lambda_{2n}^{n-1}\psi_{2n} & \lambda_{2n}^{n}\psi_{2n} \end{vmatrix},$$

$$(\Omega_n)_{22}=\begin{vmatrix} 0 & 1 & 0 & \lambda & \cdots & 0 & \lambda^{n-1} & \lambda^{n} \\ \varphi_1 & \psi_1 & \lambda_1\varphi_1 & \lambda_1\psi_1 & \cdots & \lambda_1^{n-1}\varphi_1 & \lambda_1^{n-1}\psi_1 & \lambda_1^{n}\psi_1 \\ \varphi_2 & \psi_2 & \lambda_2\varphi_2 & \lambda_2\psi_2 & \cdots & \lambda_2^{n-1}\varphi_2 & \lambda_2^{n-1}\psi_2 & \lambda_2^{n}\psi_2 \\ \vdots & \vdots & \vdots & \vdots & \vdots & \vdots & \vdots & \vdots \\ \varphi_{2n} & \psi_{2n} & \lambda_{2n}\varphi_{2n} & \lambda_{2n}\psi_{2n} & \cdots & \lambda_{2n}^{n-1}\varphi_{2n} & \lambda_{2n}^{n-1}\psi_{2n} & \lambda_{2n}^{n}\psi_{2n} \end{vmatrix}.$$

For the n-fold Darboux transformation, the transformed potentials are

$$\Lambda^{[n]}=\Lambda+[J,T_n], \tag{A6}$$

which produce the following n-order solutions

$$q^{[n]}=q^{[0]}-2\,i\,\frac{(M_1)_{12}}{\sqrt{R(z)/d_2(z)}}. \tag{A7}$$

Note that

$$\lambda_{2k}=-\lambda_{2k-1}^{*},\quad \Phi_{2k}=\begin{pmatrix}\varphi_{2k}\\ \psi_{2k}\end{pmatrix}=\begin{pmatrix}-\psi_{2k-1}^{*}\\ \varphi_{2k-1}^{*}\end{pmatrix}, \tag{A8}$$

in order to hold the constraints of the n-fold Darboux transformation.

[1] N. Akhmediev and A. Ankiewicz, *Solitons, Nonlinear Pulses and Beams* (Chapman and Hall, London, 1997).

[2] N. Akhmediev, A. Ankiewicz, and M. Taki, Phys. Lett. A **373**, 675 (2009).

[3] B. Kibler, J. Fatome, C. Finot, G. Millot, G. Genty, B. Wetzel, N. Akhmediev, F. Dias, and J. M. Dudley, Sci. Rep. **2**, 463 (2012).

[4] J. M. Dudley, F. Dias, M. Erkintalo, and G. Genty, Nature Photon. **8**, 755 (2014); A. Chabchoub, B. Kibler, J. M. Dudley, and N. Akhmediev, Philos. Trans. R. Soc. London A **372**, 20140005 (2014).

[5] D. H. Peregrine, J. Aust. Math. Soc. Series B **25**, 16 (1983); K. L. Henderson, D. H. Peregrine, and J. W. Dold, Wave Motion **29**, 341 (1999); C. Kharif, E. Pelinovsky, and A. Slunyaev, *Rogue Waves in the Ocean* (Springer-Verlag, Berlin, 2009).

[6] V. I. Shrira and V. V. Geogjaev, J. Eng. Math. **67**, 11 (2010).

[7] V. E. Zakharov and L. A. Ostrovsky, Physica D **238**, 540 (2009); V. E. Zakharov and A. A. Gelash, Phys. Rev. Lett. **111**, 054101 (2013).

[8] M. Onorato, S. Residori, U. Bortolozzo, A. Montina, and F. T. Arecchi, Phys. Rep. **528**, 47 (2013).

[9] F. Baronio, M. Conforti, A. Degasperis, S. Lombardo, M. Onorato, and S. Wabnitz, Phys. Rev. Lett. **113**, 034101 (2014); F. Baronio, S. Chen, P. Grelu, S. Wabnitz, and M. Conforti, Phys. Rev. A **91**, 033804 (2015).

[10] B. Kibler, J. Fatome, C. Finot, G. Millot, F. Dias, G. Genty, N. Akhmediev, and J. M. Dudley, Nature Phys. **6**, 790 (2010).

[11] A. Chabchoub, N. P. Hoffmann, and N. Akhmediev, Phys. Rev. Lett. **106**, 204502 (2011).

[12] H. Bailung, S. K. Sharma, and Y. Nakamura, Phys. Rev. Lett. **107**, 255005 (2011).

[13] F. Abdullaev, S. Darmanyan, and P. Khabibullaev, *Optical Solitons* (Springer, Berlin, 1991).

[14] G. P. Agrawal, *Nonlinear Fiber Optics*, 3rd ed. (Academic Press, San Diego, 2002).

[15] M. Li, B. Tian, W. J. Liu, H. Q. Zhang, X. H. Meng, and T. Xu, Nonlinear Dyn. **62**, 919 (2010).

[16] S. Chakraborty, S. Nandy, and A. Barthakur, Phys. Rev. E **91**, 023210 (2015).

[17] V. N. Serkin and A. Hasegawa, Phys. Rev. Lett. **85**, 4502 (2000).

[18] V. N. Serkin and A. Hasegawa, IEEE J. Sel. Top. Quantum Electron. **8**, 418 (2002); V. N. Serkin, A. Hasegawa, and T. L. Belyaeva, Phys. Rev. Lett. **98**, 074102 (2007); Phys. Rev. A **81**, 023610 (2010); V. N. Serkin and T. L. Belyaeva, JETP Lett. **74**, 573 (2001).

[19] Z. Y. Yan, V. V. Konotop, and N. Akhmediev, Phys. Rev. E **82**, 036610 (2010).

[20] Z. P. Yang, W. P. Zhong, and M. R. Belic, Phys. Scr. **86**, 015402 (2012).

[21] C. Q. Dai, G. Q. Zhou, and J. F. Zhang, Phys. Rev. E **85**, 016603 (2012); W. P. Zhong, M. R. Belic, and T. W. Huang, *ibid.* **87**, 065201 (2013).

[22] L. Wang, X. Li, F. H. Qi, and L. L. Zhang, Ann. Phys. (N.Y.) **359**, 97 (2015); L. Wang, M. Li, F. H. Qi, and X. Tao, Phys. Plasmas **22**, 032308 (2015); L. Wang, M. Li, F. H. Qi, and C. Geng, Eur. Phys. J. D **69**, 108 (2015).

[23] C. G. L. Tiofack, S. Coulibaly, M. Taki, S. De Bièvre, and G. Dujardin, Phys. Rev. A **92**, 043837 (2015).

[24] W. P. Zhong, L. Chen, M. Belić, and N. Petrović, Phys. Rev. E **90**, 043201 (2014); R. B. Mareeswaran, E. G. Charalampidis, T. Kanna, P. G. Kevrekidis, and D. J. Frantzeskakis, *ibid.* **90**, 042912 (2014); S. Loomba and H. Kaur, *ibid.* **88**, 062903 (2013); C. N. Kumar, R. Gupta, A. Goyal, S. Loomba, T. S. Raju, and P. K. Panigrahi, Phys. Rev. A **86**, 025802 (2012).

[25] K. Manikandan, P. Muruganandam, M. Senthilvelan, and M. Lakshmanan, Phys. Rev. E **90**, 062905 (2014); S. Loomba, H. Kaur, R. Gupta, C. N. Kumar, and T. S. Raju, *ibid.* **89**, 052915 (2014).

[26] S. M. Guo, L. Q. Mei, and A. Sunc, Ann. Phys. (N.Y.) **332**, 38 (2012); S. M. Guo and L. Q. Mei, Phys. Plasmas **21**, 082303 (2014).

[27] R. Hirota, J. Math. Phys. **14**, 805 (1973); A. Ankiewicz, J. M. Soto-Crespo, and N. Akhmediev, Phys. Rev. E **81**, 046602 (2010).

[28] G. Y. Yang, L. Li, and S. T. Jia, Phys. Rev. E **85**, 046608 (2012).

[29] X. Wang, Y. Li, and Y. Chen, Wave Motion **51**, 1149 (2014).

[30] S. Chen and L. Y. Song, Phys. Rev. E **87**, 032910 (2013).

[31] H. N. Chan, K. W. Chow, D. J. Kedziora, R. H. J. Grimshaw, and E. Ding, Phys. Rev. E **89**, 032914 (2014).

[32] A. Chowdury, A. Ankiewicz, and N. Akhmediev, Proc. R. Soc. London A **471**, 20150130 (2015).

[33] A. Chowdury, D. J. Kedziora, A. Ankiewicz, and N. Akhmediev, Phys. Rev. E **91**, 032928 (2015).

[34] L. Wang, J. H. Zhang, Z. Q. Wang, C. Liu, M. Li, F. H. Qi, and R. Guo, Phys. Rev. E **93**, 012214 (2016).

[35] L. Wang, Y. J. Zhu, Z. Q. Wang, T. Xu, F. H. Qi, and Y. S. Xue, J. Phys. Soc. Jpn. **85**, 024001 (2016).

[36] L. Wang, S. Li, and F. H. Qi, Nonlinear Dynam. (to be published).

[37] L. H. Wang, K. Porsezian, and J. S. He, Phys. Rev. E **87**, 053202 (2013).

[38] C. Liu, Z. Y. Yang, L. C. Zhao, and W. L. Yang, Phys. Rev. E **91**, 022904 (2015).

[39] C. Liu, Z. Y. Yang, L. C. Zhao, and W. L. Yang, Ann. Phys. (N.Y.) **362**, 130 (2015).

[40] R. C. Yang, L. Li, R. Y. Hao, Z. H. Li, and G. S. Zhou, Phys. Rev. E **71**, 036616 (2005).

[41] P. Wong, W. J. Liu, L. G. Huang, Y. Q. Li, N. Pan, and M. Lei, Phys. Rev. E **91**, 033201 (2015).

[42] J. S. He, Y. S. Tao, K. Porsezian, and A. S. Fokas, J. Nonlinear Math. Phy. **20**, 407 (2013).

[43] X. Wang and Y. Chen, arXiv:1512.07938v1.

[44] Y. Ren, Z. Y. Yang, C. Liu, and W. L. Yang, Phys. Lett. A **379**, 2991 (2015).

[45] L. Wang, Z. Q. Wang, J. H. Zhang, F. H. Qi, and M. Li, arXiv:1601.07029v1.

[46] Yu. S. Kivshar, Phys. Rev. A **43**, 1677 (1991); Yu. S. Kivshar and V. V. Afanasjev, *ibid.* **44**, R1446(R) (1991).

[47] J. F. Zhang, Q. Yang, and C. Q. Dai, Opt. Commun. **248**, 257 (2005).

[48] A. Ankiewicz, J. M. Soto-Crespo, M. A. Chowdhury, and N. Akhmediev, J. Opt. Soc. Am. B **30**, 87 (2013).

[49] C. Liu, Z. Y. Yang, L. C. Zhao, L. Duan, G. Yang, and W. L. Yang, arXiv:1603.04554v1.

[50] M. Droques, A. Kudlinski, G. Bouwmans, G. Martinelli, and A. Mussot, Opt. Lett. **37**, 4832 (2012); Phys. Rev. A **87**, 013813 (2013).

[51] S. Li, L. Li, Z. Li, and G. Zhou, J. Opt. Soc. Am. B **21**, 2089 (2004).